

# Fermionic-Adapted Shadow Tomography for dynamical correlation functions

Taehee Ko,<sup>1,\*</sup> Mancheon Han,<sup>1</sup> Hyowon Park,<sup>2,3</sup> and Sangkook Choi<sup>1,†</sup>

<sup>1</sup>*School of Computational Sciences, Korea Institute for Advanced Study*

<sup>2</sup>*Materials Science Division, Argonne National Laboratory, Argonne, IL, 60439, USA*

<sup>3</sup>*Department of Physics, University of Illinois at Chicago, Chicago, IL, 60607, USA*

## Abstract

Dynamical correlation functions are essential for characterizing the response of quantum many-body systems to external perturbation. As their calculation is classically intractable in general, quantum algorithms are promising in this aspect, but most rely on brute force measurement strategies that evaluate one body observable pair per circuit. In this work, we introduce Fermionic-Adapted Shadow Tomography (FAST) protocols, a new framework for the efficient calculation of multiple dynamical correlation functions. The key idea is to reformulate these functions into forms that are compatible with shadow tomography techniques. The circuits in our protocols require at most two-copy measurements with uncontrolled Hamiltonian simulation. We show that the proposed protocols enhance sample efficiency and/or reduce the number of measurement circuits by one or two orders of magnitude with respect to the system size across a range of scenarios.

## INTRODUCTION

The simulation of quantum many-body systems is considered as one of the most promising areas for realizing quantum advantage [1–4]. Among various applications, of critical interest in computational physics is the estimation of dynamical correlation functions. Since they formulate physical properties for measured outcomes from experiments [5], developing efficient simulation tools for the correlation functions is of practical importance for understanding the physics behind systems in experiments. Besides, correlation functions are the building-block for the functional approaches to the quantum many-body theory [6–8].

For the task, numerous quantum algorithms have been proposed recently. Roughly, the algorithms are classified into variational and sampling-based approaches. Variational approaches optimize parameterized circuits to approximate the correlation functions, which is suitable for near-term quantum computers [9–13]. Alternatively, sampling-based approaches enable the estimation of correlation functions using guaranteed numerical techniques. These include the Hadamard test combined with the Hamiltonian simulation [14–18] or the block encoding [19]. In these algorithms, a correlation function is estimated at a given time or frequency point.

Notably, measurements with sophisticated circuit constructions or techniques can facilitate the computation of correlation functions. For example, computing the functions at multiple time points is performed with a single circuit [20–22], and the methods in [23, 24] apply shadow tomography techniques for computing multiple correlation functions at a time point. A key insight from these approaches is that building clever measurement strategies can lead to efficient and novel algorithms, an idea already explored in a variety of applications such as efficient measurement schemes for

---

\* [kthmomo@kias.re.kr](mailto:kthmomo@kias.re.kr)

† [sangkookchoi@kias.re.kr](mailto:sangkookchoi@kias.re.kr)

variational quantum algorithms [25–31], measurement-based quantum computing algorithms [32–36], and shadow tomography techniques for learning tasks [3, 23, 37–40].

Particularly in condensed matter theory and quantum chemistry, estimating multiple dynamical correlation functions is an essential task, as the number of those often scales polynomially with system size. Examples include the retarded Green’s function and the density-density correlation, for which the number of correlation functions scales quadratically and quartically, respectively [5]. Under a brute-force measurement strategy, these scalings translate directly into the overall sample complexity and the number of measurement circuits. Recently, several methods have been proposed to simultaneously estimate dynamical correlation functions, such as Green’s function estimation using shadow tomography techniques [23, 24] and more general functions using a phase kickback technique [21]. Still, a sample-efficient and practically viable framework for simultaneously estimating many dynamical correlation functions remains lacking.

In this work, we introduce a new framework for efficiently estimating the dynamical correlation functions via shadow tomography techniques. We first reformulate the correlation functions into direct measurement forms that enable to incorporate shadow tomography techniques. We refer to our protocols as Fermionic-Adapted Shadow Tomography (FAST). The FAST is classified into the commutator and anti-commutator cases. For the commutator correlation functions, the FAST achieves at least order one of reduction with respect to the number of fermionic modes  $n$  in terms of sample complexity and the number of circuits to execute. In the anti-commutator case, in the regime where  $n \geq \frac{1}{\epsilon^2}$  for a given precision  $\epsilon$ , the FAST achieves improvement compared to the brute force measurement in terms of sample complexity and the number of circuits to execute by an order of magnitude. When  $n \leq \frac{1}{\epsilon^2}$ , the FAST can reduce the number of circuits an order of magnitude but does not improve sample complexity.

Throughout this work, we do not consider various noises in quantum hardware, which is beyond the scope of this work. Accordingly, we make the assumption that the circuits in Fig. 1 are implemented on a fault-tolerant quantum computer. Additionally, a problem-dependent state  $\rho$  is provided, along with uncontrolled Hamiltonian simulation. The main operations in the circuits Fig. 1 involve the preparation of a problem-dependent quantum state [41–47] (e.g. the ground state of system), the compilation of uncontrolled Hamiltonian simulations [43, 48–52], and the dynamical circuit strategy in [33]. The first two operations are among the most actively studied areas in quantum computing. The dynamical circuit strategy in [33] allows a single circuit to conduct the random Pauli measurement [3]. Recent advances in quantum hardware are making the implementation of dynamic circuits progressively more practical [53–55].

Under this assumption, we address a central question: can we develop more efficient protocols for estimating the dynamical correlation functions than the brute force strategy of measuring one-body observable pairs at a time, specifically in terms of sample complexity and/or the number of measurement circuits? We answer this by proposing protocols tailored to each of the representative fermion-to-qubit mappings: Jordan-Wigner (JW), Bravyi-Kitaev (BK) [56], and ternary tree (TT) [57].

## RESULTS

### Related work

Several works have demonstrated the estimation of Green’s function using Hadamard-test circuits [9–11, 13], based on strategies of brute-force measurements. These methods require two controlled Pauli operators in estimating real-time Green’s functions, together with a time evolution block or

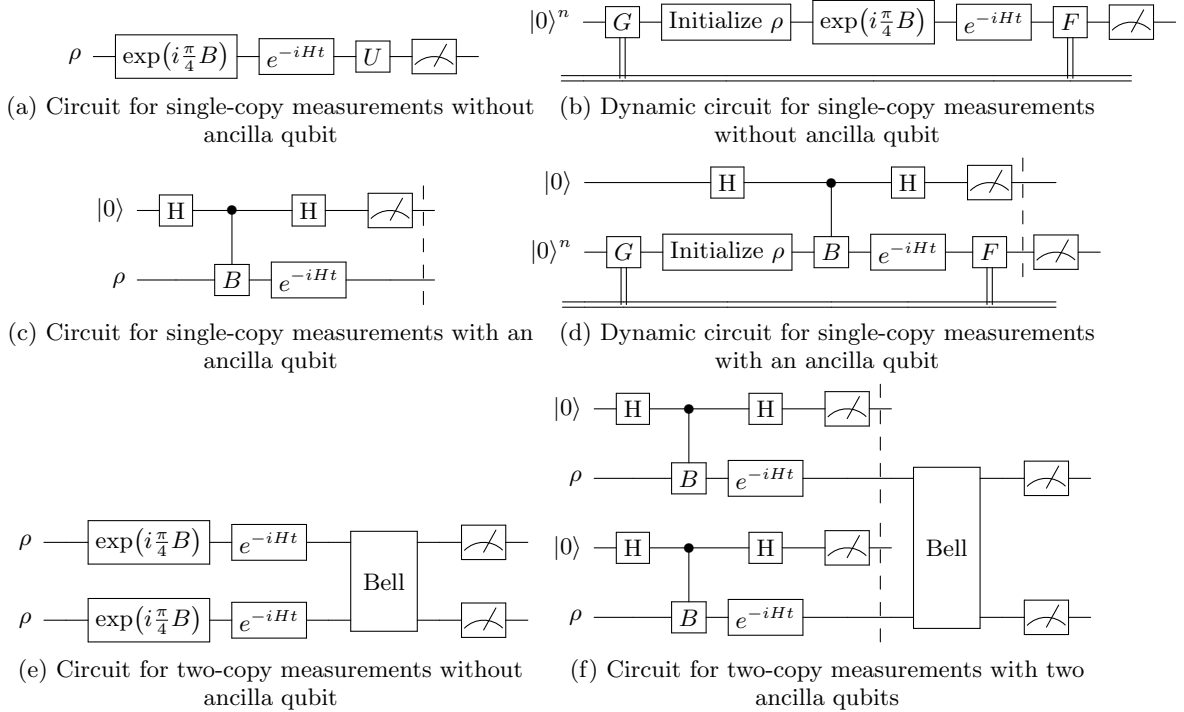


FIG. 1: Circuits for single-copy and two-copy measurements used in our protocols for estimating the dynamical correlation functions. The gate  $B$  denotes a given Pauli string. In Fig. 1a, a set of Clifford unitaries for mutually commuting observables, denoted as  $U$ , is used. In Fig. 1b, Fig. 1d, we use the dynamic circuit technique for random Pauli measurement [33]. Following the same notation in [33], we denote by  $G, F$ , the operations for generating the probability distribution for which Pauli basis is sampled, and receiving the feedback for constructing the corresponding Pauli basis. In Fig. 1e, we perform the Bell sampling to throw out observables of negligible expectation magnitudes [23, 58]. In Fig. 1f, we also apply Bell sampling in a certain case, while in the other, we use a variant that requires measurement in a problem-dependent basis, as will be shown in Lemma 6.

a corresponding parameterized circuit block. Since the two Pauli operators arise in the expansion of Green's function, the number of measurement circuits and the total sample complexity scales as  $\mathcal{O}(n^2)$  and  $\mathcal{O}(\frac{n^2 \log n}{\epsilon^2})$ , respectively, where  $n$  denotes the system size. The recent works [23, 24] propose methods for estimating Green's functions using shadow tomography techniques. While their target calculations are slightly different (i.e. [23] for a fixed time and [24] for a fixed frequency), the common idea is that reformulating correlation functions enables the use of shadow tomography techniques and the savings of measurement cost. The algorithm in [24] is based on a continued fraction of the Green's function and outputs single and multiple Green's functions. In their approach, the number of observables scales exponentially with the level of continued fraction, so efficient measurements are considered such as classical shadow and fermionic shadow. On the other hand, the approach in [23] uses the Taylor expansion of Green's function and requires to compute derivatives at time zero. Their approach requires at least  $\mathcal{O}(n^3)$  time because of the entangled measurement

constructions [59]. Especially for typical Hamiltonian models where the number of Majorana operators scales linearly with the system size, such as the Hubbard model, the time complexity is expected to scale as  $\Omega(n^3)$  due to the processing time to estimate nested commutator terms, and the number of measurement circuits may scale as  $\Omega(\frac{n}{\epsilon^2})$  since at least one-body observables have to be estimated in the process. In contrast to these methods, our approach considers both regimes:  $n \leq \frac{1}{\epsilon^2}$  and  $n \geq \frac{1}{\epsilon^2}$ . In both cases, it can reduce the number of circuits by an order of magnitude and improves sample complexity, especially in the regime  $n \geq \frac{1}{\epsilon^2}$ . Additionally, our approach maintains a post-processing time comparable to that of brute-force methods, and it can estimate Green's functions across a similar range of time points using identical time-evolution blocks. Table I details the complexity measures across brute-force measurements [9–11, 13], the shadow method in [23], and our proposed approach.

Compared to the case of Green's function, fewer results exist for estimating bosonic correlation functions via quantum computation [11, 14, 16]. With explicit circuit constructions, [16] proposes an approach for estimating response functions in the frequency domain, but the computational complexity of their approach scales exponentially with system size, due to calculations for all eigenvalues. More closely related to our work are the time-domain approaches [11, 14]. The method in [14] provides an ancilla-free implementation using time-dependent Hamiltonian simulations within a linear response framework, whereas [11] employs Hadamard-test circuits with multiple controlled operations to estimate general susceptibilities. Generally, these approaches incur an  $\mathcal{O}(n^4 \log n)$  sample complexity and a similarly scaling number of measurement circuits. By leveraging shadow tomography, our approach reduces this quartic scaling to cubic or better, depending on the regime. Moreover, similar to [14], our method avoids controlled Pauli operations entirely. For all three time-domain approaches,  $\mathcal{O}(n^4)$  correlation functions are evaluated from measurement outcomes, yielding an  $\mathcal{O}(n^4)$  post-processing time. Table II summarizes this comparison between our method and those in [11, 14].

Our technical contributions are summarized as follows:

- We derive identities (9), (12), and (13), which establish a general framework for estimating both commutator and anti-commutator dynamical correlation functions. Our approach is naturally compatible with various shadow tomography techniques, without controlled time evolution.
- (Commutator case) By integrating measurement techniques in [30] and [23] into our framework, we achieve a significant reduction in both sample complexity and the number of measurement circuits. For the regime  $n \leq \frac{1}{\epsilon^2}$  using TT mapping, we introduce a new measurement strategy (Lemma 3) combining classical shadows [3] and dynamic circuits [33]. This approach reduces circuit construction time and measurement overhead by at least an order of magnitude relative to system size compared to previous results [11, 14].
- (Anti-commutator case) We provide tailored strategies for the anti-commutator based on the mapping and regime. In the regime  $n \leq \frac{1}{\epsilon^2}$ , our protocol reduces only the number of circuits by an order of magnitude with respect to system size. In the other regime  $n \geq \frac{1}{\epsilon^2}$ , we introduce two measurement strategies. The first is optimized for BK and TT mappings (Lemma 5), while the second is designed for JW mapping (Lemma 6). For the JW case, we develop a novel two-copy measurement strategy that reduces the required number of circuits by a factor of  $1/\epsilon^2$  relative to our first strategy.

Method	[9–11, 13]	[23]	This work	
Measurement type	Brute-force	Shadow-based	Shadow-based	
Target calculation	$\{G_{ab}(t)\}_{a,b=1}^n$	$\{G_{ab}^{(q)}(0)\}_{a,b=1}^n$	$\{G_{ab}(t)\}_{a,b=1}^n$	
Regime	$n \geq 1$	$n \geq \frac{1}{\epsilon^2}, t \approx 0$	$n \leq \frac{1}{\epsilon^2}$	$n \geq \frac{1}{\epsilon^2}$
Sample complexity <sup>a</sup>	$\mathcal{O}(\frac{n^2 \log n}{\epsilon^2})$	$\mathcal{O}(\frac{(nq)^{5q} \log n}{\epsilon^4})$	$\mathcal{O}(\frac{n^2 \log n}{\epsilon^2})$	$\mathcal{O}(\frac{n \log n}{\epsilon^4})$
Ancilla qubit	1	0	1	2
the number of copies of $\rho$	1	2	1	2
the number of circuits	$\mathcal{O}(n^2)$	$\Omega(\frac{n}{\epsilon^2})$	$\mathcal{O}(n^2)$ (JW,BK) or $\mathcal{O}(n)$ (TT)	$\mathcal{O}(n)$
Measurement circuit depth	$\mathcal{O}(1)$	$\mathcal{O}(n)$	$\mathcal{O}(1)$	$\mathcal{O}(1)$
Controlled Pauli operation	2	0	1	2
Time evolution block <sup>b</sup>	1	0	1	2
Classical post-processing	$\mathcal{O}(n^2)$	$\Omega(n^3)$	$\mathcal{O}(n^2)$	$\mathcal{O}(n^2)$

<sup>a</sup> We consider typical Hamiltonian models such as the Hubbard model, where  $s = \mathcal{O}(n)$ . This affects the sparsity parameter in [23, Definition B.2].

<sup>b</sup> Parameterized circuit blocks in [9–11, 13] are considered as time evolution blocks

TABLE I: Comparison between the methods in [9–11, 13], the method in [23, Theorem B.1], and our method, towards the calculation of the Green’s function  $G_{ab}(t) = -i \text{tr}(\rho\{c_i(t), c_j^\dagger\})$ . As a subroutine, the approach in [23] estimates the  $q$ -th order derivative of Green’s function. ”Controlled Pauli operation” indicates the number of controlled Pauli operations that apply a Pauli string,  $P$ , on the target register. ”Time evolution block” corresponds to a query of the Hamiltonian simulation. ”Classical post-processing” means the time spent on thresholding small measurement values and evaluating the  $\mathcal{O}(n^2)$  correlation functions from measurement values.

### Reformulations of correlation functions

We consider two types of dynamical correlation functions:

$$C(A, B, t) = \text{tr}(\rho[A(t), B]) \text{ or } \text{tr}(\rho\{A(t), B\}). \quad (1)$$

Here,  $A$  and  $B$  can be represented by Pauli strings under a fermion-to-qubit mapping, corresponding to fermionic or Majorana operators. These lattice correlation functions form a building block for the real-space correlation function:

$$C(\mathbf{r}, \mathbf{r}', t) = \sum_{A, B} \Phi_A(\mathbf{r}) \Phi_B(\mathbf{r}') C(A, B, t). \quad (2)$$

Here,  $\Phi_A(\mathbf{r})$  denotes the mode wavefunction spanning in the Hilbert space for the operator  $A$ .

**Example 1** (Green’s functions). *The retarded Green’s function is defined as*

$$G_{ij}^R(t) = -i\theta(t) \text{tr}(\rho\{c_i(t), c_j^\dagger(0)\}), \quad (3)$$

where  $c_i(t) = e^{iHt} c_i e^{-iHt}$  is the fermionic annihilation operator in the Heisenberg picture. This lattice Green’s function is used to calculate real space Green’s function:

$$G^R(\mathbf{r}, \mathbf{r}', t) = \sum_{i, j} \varphi_i(\mathbf{r}) \varphi_j^*(\mathbf{r}') G_{ij}^R(t), \quad (4)$$

Method	[11]	[14]	This work	
Measurement type	Brute-force	Brute-force	Shadow-based	
Target calculation	$\{F_{ijkl}(t)\}_{i,j,k,l=1}^n$			
Regime	$n \geq 1$	$n \geq 1$	$n \leq \frac{1}{\epsilon^2}$	$n \geq \frac{1}{\epsilon^2}$
Sample complexity	$\mathcal{O}(\frac{n^4 \log n}{\epsilon^2})$	$\mathcal{O}(\frac{n^4 \log n}{\epsilon^2})$	$\mathcal{O}(\frac{n^3 \log n}{\epsilon^2})$	$\mathcal{O}(\frac{n^2 \log n}{\epsilon^4})$
Ancilla qubit	1	0	0	0
the number of copies of $\rho$	1	1	1	2
the number of circuits	$\mathcal{O}(n^4)$	$\mathcal{O}(n^4)$	$\mathcal{O}(n^3)$ (JW,BK) or $\mathcal{O}(n^2)$ (TT)	$\mathcal{O}(\frac{n^2}{\epsilon^2})$
Measurement circuit depth	$\mathcal{O}(1)$	$\mathcal{O}(1)$	$\mathcal{O}(n)$ (JW,BK) or $\mathcal{O}(1)$ (TT)	$\mathcal{O}(n)$
Controlled Pauli operation <sup>a</sup>	4	0	0	0
Time evolution block <sup>b</sup>	1	1	1	2
Classical post-processing	$\mathcal{O}(n^4)$	$\mathcal{O}(n^4)$	$\mathcal{O}(n^4)$	$\mathcal{O}(n^4)$

<sup>a</sup> We let  $P_4, P_5$  be the identities in [11, Figure 2(a)]

<sup>b</sup> We plug  $t = 0$  in [11, Figure 2(a)] for the comparison

TABLE II: Comparison between the method in [11] and our method for the calculation of the correlation function  $F_{ijkl}(t) = \text{tr}(\rho[e^{iHt}c_i^\dagger c_j e^{-iHt}, c_k^\dagger c_l])$ . We use the same metrics as in Table I.

Notation	Description
$c_i^\dagger, c_i$	Fermionic creation and annihilation operators on mode $i \in [n]$
$\{c_i, c_j^\dagger\} = \delta_{ij}$	Canonical anticommutation relations
$\{c_i, c_j\} = 0$	Fermionic annihilation anticommutation relation
$O(t) := e^{iHt} O e^{-iHt}$	Heisenberg time evolution of operator $O$
$\gamma_{2i-1} = c_i + c_i^\dagger$	Majorana operator (real component)
$\gamma_{2i} = i(c_i - c_i^\dagger)$	Majorana operator (imaginary component)
$\{\gamma_a, \gamma_b\} = 2\delta_{ab}$	Majorana anticommutation relations
$B$	Operator represented as Pauli strings or sums of Pauli strings (context-dependent)
$P = \bigotimes_{k=1}^n \sigma_k^{\alpha_k}$	$n$ -qubit Pauli string
$\sigma^\alpha \in \{I, X, Y, Z\}$	Single-qubit Pauli operators

TABLE III: Summary of notation used throughout the paper.

where  $\varphi_i(\mathbf{r})$  is the wavefunction for the mode index  $i$ . This real space Green's function is central to the computation of spectral functions and local density of states via the Fourier transform.

**Example 2** (Density-Density Response). Let  $n_i = c_i^\dagger c_j$  be the density matrix operators. Then, the lattice density-density correlation function is

$$\chi_{ij;kl}(t) = -i\theta(t) \text{tr}(\rho[n_{ij}(t), n_{kl}(0)]), \quad (5)$$

which is used to compute the real space density-density response,

$$\chi(\mathbf{r}, \mathbf{r}', t) = \sum_{ij;kl} \varphi_i^*(\mathbf{r}) \varphi_j(\mathbf{r}) \varphi_k^*(\mathbf{r}') \varphi_l(\mathbf{r}') \chi_{ij;kl}(t). \quad (6)$$

This function measures how a density perturbation at  $\mathbf{r}'$  affects the density at  $\mathbf{r}$  at a later time.

We notice that the correlation function of the form (1) is decomposed into

$$\mathrm{tr}(\rho[A(t), B]) = \sum_{m=1}^M b_m \mathrm{tr}(\rho[A(t), B_m]) \quad \text{or} \quad \mathrm{tr}(\rho\{A(t), B\}) = \sum_{m=1}^M b_m \mathrm{tr}(\rho\{A(t), B_m\}), \quad (7)$$

if  $B = \sum_{m=1}^M b_m B_m$ . For our applications,  $B_m$  denotes a Pauli string. When  $B$  is a 1-body fermionic observable or a creation operator (e.g. the examples below (1)),  $M = \mathcal{O}(1)$  and  $b_m = \mathcal{O}(1)$  for each  $m$ , under a fermion-to-qubit mapping [9, 10].

From this observation, we present reformulations of the correlation functions in (1), focusing on the case where  $B$  is a Pauli string. The general case where  $B = \sum_{m=1}^M b_m B_m$  can be straightforwardly resolved by repeating those reformulations  $M$  times and summing them up.

In the commutator case, we reformulate the representation of the correlation functions as,

$$\begin{aligned} C(A, B, t) &= \mathrm{tr}(\rho[A(t), B]) \\ &= -i \left[ 4 \mathrm{tr} \left( \left( \frac{I + iB^\dagger}{2} \right) \rho \left( \frac{I - iB}{2} \right) A(t) \right) - \mathrm{tr}(\rho A(t)) - \mathrm{tr}(B^\dagger \rho B A(t)) \right]. \end{aligned} \quad (8)$$

If  $B$  is a Pauli string, we can simplify this formulation to

$$C(A, B, t) = -i \left[ 2 \mathrm{tr}(e^{-iHt} e^{i\frac{\pi}{4}B} \rho e^{-i\frac{\pi}{4}B} e^{iHt} A) - \mathrm{tr}(e^{-iHt} \rho e^{iHt} A) - \mathrm{tr}(e^{-iHt} B \rho B e^{iHt} A) \right] \quad (9)$$

Therefore, this representation allows us to estimate the commutator correlation function with three types of direct measurements and three circuits: 1. measure observable  $A$  with state  $e^{-iHt} e^{i\frac{\pi}{4}B} \rho e^{-i\frac{\pi}{4}B} e^{iHt}$ , 2. measure observable  $A$  with state  $e^{-iHt} \rho e^{iHt}$ , and 3. measure observable  $A$  with state  $e^{-iHt} B \rho B e^{iHt}$ .

However, the anti-commutator case is not straightforward as the commutator case. To do similarly, we require the operation  $\frac{I+B}{2}$  or  $\frac{I-B}{2}$  as shown below but these are non-unitary operations that are not directly implementable on quantum computers. In this case, we therefore introduce a measurement-based strategy, which leads to two representations of the anti-commutator correlation function. By a bit of algebra, we achieve that

$$\begin{aligned} C(A, B, t) &= \mathrm{tr}(\rho\{A(t), B\}) \\ &= 4 \mathrm{tr} \left( \left( \frac{I + B}{2} \right) \rho \left( \frac{I + B}{2} \right) A(t) \right) - \mathrm{tr}(\rho A(t)) - \mathrm{tr}(B \rho B A(t)), \end{aligned} \quad (10)$$

and

$$\begin{aligned} C(A, B, t) &= \mathrm{tr}(\rho\{A(t), B\}) \\ &= -4 \mathrm{tr} \left( \left( \frac{I - B}{2} \right) \rho \left( \frac{I - B}{2} \right) A(t) \right) + \mathrm{tr}(\rho A(t)) + \mathrm{tr}(B \rho B A(t)). \end{aligned} \quad (11)$$

Equivalently, we observe that

$$\begin{aligned} C(A, B, t) &= 4C_+^2 \mathrm{tr}(\rho_+ A) - \mathrm{tr}(e^{-iHt} \rho e^{iHt} A) - \mathrm{tr}(e^{-iHt} B \rho B e^{iHt} A) \\ C_+^2 &= \mathrm{tr} \left( \left( \frac{I + B}{2} \right) \rho \left( \frac{I + B}{2} \right) \right), \quad \rho_+ = \frac{e^{-iHt} \left( \frac{I+B}{2} \right) \rho \left( \frac{I+B}{2} \right) e^{iHt}}{C_+}, \end{aligned} \quad (12)$$

and

$$C(A, B, t) = -4C_-^2 \text{tr}(\rho_- A) + \text{tr}(e^{-iHt} \rho e^{iHt} A) + \text{tr}(e^{-iHt} B \rho B e^{iHt} A)$$

$$C_-^2 = \text{tr}\left(\left(\frac{I-B}{2}\right) \rho \left(\frac{I-B}{2}\right)\right), \rho_- = \frac{e^{-iHt} \left(\frac{I-B}{2}\right) \rho \left(\frac{I-B}{2}\right) e^{iHt}}{C_-}. \quad (13)$$

Note that  $C_+^2 + C_-^2 = 1$ . These quantities are exactly the probabilities of the output state to be  $\rho_{\pm}$ , which are obtainable from the circuits in Fig. 1c, Fig. 1d, and Fig. 1f with a controlled Pauli gate for  $B$ . Technically, we check this in (30).

We notice that the output states  $\rho_{\pm}$  from Fig. 1c, Fig. 1d, or Fig. 1f are prepared probabilistically. This implies that we cannot deterministically use the representations in (12) and (13) as the commutator case. Instead, we suggest to follow a majority rule for selecting one of the representations based on resulting statistics. Simply, for a scheduled number of circuit samplings, we count the outcomes in the ancilla. If the state  $|0\rangle$  is observed more frequently than  $|1\rangle$ , we know that  $C_+^2 \geq C_-^2$  with high probability and choose the *plus* representation (12). In the opposite case, we choose the *minus* representation (13). More importantly, we can make use of the output states at least half of the scheduled number of samplings. We state this formally in the following lemma.

**Lemma 1.** *Given scheduled  $N_s = \mathcal{O}(\frac{\log \frac{1}{\epsilon^2}}{\epsilon^2})$  circuit samplings, let  $n_+$  and  $n_-$  be the number of outcomes being  $|0\rangle$  and  $|1\rangle$  in the ancilla qubit, respectively. Then, the following holds with probability at least  $1 - \delta$ ,*

$$\left|C_+^2 - \frac{n_+}{N_s}\right|, \left|C_-^2 - \frac{n_-}{N_s}\right| \leq \epsilon, \quad (14)$$

and either  $\rho_+$  or  $\rho_-$  is prepared with at least  $\frac{N_s}{2}$  times. Consequently, in either of the fermionic correlation functions in (12) and (13), the first term can be estimated with at least  $\frac{N_s}{2}$  samples.

*Proof.* The first statement immediately follows from the Hoeffding's inequality by considering the random variable  $X$  that counts the number of outcomes to be  $|0\rangle$ . The second statement is true since  $\frac{n_+}{N_s} + \frac{n_-}{N_s} = 1$  and either of  $n_+$  or  $n_-$  must be  $\geq \frac{N_s}{2}$ , which means that one of the states  $\rho_{\pm}$  is more often returned with at least  $\frac{N_s}{2}$  samples.  $\square$

### Protocol for the commutator case

We consider the commutator correlation functions that involve 1-body observables with  $i, j, k, l \in [n]$ ,

$$\text{tr}\left(\rho[e^{iHt} c_i^\dagger c_j e^{-iHt}, c_k^\dagger c_l]\right). \quad (15)$$

In this section, we present a protocol that allows to efficiently estimate these correlation functions. The key idea is to incorporate shadow tomography techniques into the representation (9) and design protocols for the dynamical correlation functions (15).

For a given precision  $\epsilon$ , we distinguish between two regimes:  $n \leq \frac{1}{\epsilon^2}$  and  $n \geq \frac{1}{\epsilon^2}$ . This is motivated by the recent result by King *et al* [23]. We first consider the case when  $n \leq \frac{1}{\epsilon^2}$  and JW or BK mapping is applied. The following lemma is an immediate extension of fermionic partition strategy in [30] as we prove in the following.

**Lemma 2.** *Assume  $n \leq \frac{1}{\epsilon^2}$ . Then, there exists a shadow tomography protocol that is compatible with the Jordan-Wigner (JW) mapping and the Bravyi-Kitaev (BK) mapping, and uses single-copy measurements to estimate the 1-body fermionic observables to additive error  $\epsilon$  with sample complexity,*

$$\mathcal{O}\left(\frac{n \log n}{\epsilon^2}\right), \quad (16)$$

and  $\mathcal{O}(n)$  measurement circuits of  $\mathcal{O}(n)$  depth.

*Proof.* From a fermionic partition strategy [30], we can construct  $\mathcal{O}(n)$  clifford measurement circuits for measuring products of two Majorana operators, with  $\mathcal{O}(n)$  depth. Since

$$c_i^\dagger c_j = (\gamma_{2i-1} + i\gamma_{2i})(\gamma_{2j-1} - i\gamma_{2j}), \quad (17)$$

we notice that the 1-body fermionic observable is formed by a sum of four 2-Majorana operators, and therefore measuring the 1-body fermionic observables requires  $\mathcal{O}(n)$  circuits with  $\mathcal{O}(n)$  depth.  $\square$

Now we consider the situation where  $n \leq \frac{1}{\epsilon^2}$  and TT mapping [57] is applied. Compared to the BK mapping that achieves  $\log_2 n + 1$  locality [60] as the worst-case, the TT mapping improves the base factor as  $\log_3(2n)$  locality. In turn, this enables estimating the 1-body observables with comparable sample complexity to the protocol in Lemma 2 by incorporating it into the random Pauli measurement in [3]. We can further make it practical for real quantum execution by employing the notion of dynamic circuits [33], which allows to do the task with a single circuit in principle. We summarize this protocol in the following lemma.

**Lemma 3.** *Assume that  $n \leq \frac{1}{\epsilon^2}$ . Then, there exists a shadow tomography protocol that is compatible with the ternary tree (TT) mapping, and uses single-copy measurements to estimate the 1-body observables to additive error  $\epsilon$  with sample complexity,*

$$\mathcal{O}\left(\frac{n \log n}{\epsilon^2}\right), \quad (18)$$

and  $\mathcal{O}(1)$  measurement circuits of  $\mathcal{O}(1)$  depth.

*Proof.* Since the TT mapping yields  $\log_3(2n)$ -local Pauli strings for the Majorana operators, and the sample complexity of the random Pauli measurement [3] scales as  $\mathcal{O}\left(\frac{3^w \log m}{\epsilon^2}\right)$  where  $w$  is the locality of Pauli string and  $m$  is the number of observables, the sample complexity of estimating the 1-body observables is  $\mathcal{O}\left(\frac{n \log n}{\epsilon^2}\right)$ , as we deduced in the proof of Lemma 2. Furthermore, the dynamic circuit [33] allows to perform the random Pauli measurements with  $\mathcal{O}(1)$  measurement circuits.  $\square$

For the case where  $n \geq \frac{1}{\epsilon^2}$ , we use the results from [23] as restated in the following lemma.

**Lemma 4.** [23, from Lemmas 1.1 and 4.1] *Assume that  $n \geq \frac{1}{\epsilon^2}$ . Then, there exists a shadow tomography protocol that is compatible with the JW, BK, and TT mappings, uses  $\mathcal{O}\left(\frac{1}{\epsilon^2}\right)$  circuits, single-copy and two-copy measurements to estimate the 1-body observables to additive error  $\epsilon$  with sample complexity,*

$$\mathcal{O}\left(\frac{\log n}{\epsilon^4}\right), \quad (19)$$

and the depth of each circuit scales as  $\mathcal{O}(n)$  at most.

For concreteness, the proof of this lemma is shown below Lemma 8, which immediately follows from the original work [23].

By applying these results, we obtain a shadow tomography protocol for estimating the correlation functions in (15) as follows,

**Theorem 1.** *For a given precision  $\epsilon > 0$ , there exists a shadow tomography protocol that is compatible with the JW, BK, and TT mappings, uses at most two-copy measurements, and estimates the correlation functions in (15) to the precision  $\epsilon$  with the following complexity:*

- if  $n \leq \frac{1}{\epsilon^2}$ , the sample complexity scales as  $\mathcal{O}(\frac{n^3 \log n}{\epsilon^2})$  with  $\mathcal{O}(n^3)$  (JW, BK) and  $\mathcal{O}(n^2)$  (TT) measurement circuits.
- if  $n \geq \frac{1}{\epsilon^2}$ , the sample complexity scales as  $\mathcal{O}(\frac{n^2 \log n}{\epsilon^4})$  with  $\mathcal{O}(\frac{n^2}{\epsilon^2})$  measurement circuits.

*Proof.* In the representation (15), we fix  $k, l$ . Then, for any given fermion-to-qubit mapping among JW, BK, and TT, we can transform the observable  $c_k^\dagger c_l$  into a sum of four Pauli strings. This yields an expression similar to the commutator case in (7). Now it reduces to estimating the following quantity from (15)

$$\text{tr}\left(\rho[e^{iHt}c_i^\dagger c_j e^{-iHt}, B]\right) \quad (20)$$

for a Pauli string  $B$  from  $c_k^\dagger c_l$ . Using the representation (9) and setting  $A = c_i^\dagger c_j$ , we apply the results in Lemma 2 (JW,BK), Lemma 3 (TT), and Lemma 4 (JW,BK,TT) to estimate  $A$  with  $i, j \in [n]$ , by considering the following three measurements

$$\begin{aligned} \text{tr}(\rho_1 A), \quad \rho_1 &= e^{-iHt} e^{i\frac{\pi}{4}B} \rho e^{-i\frac{\pi}{4}B} e^{iHt} \\ \text{tr}(\rho_2 A), \quad \rho_2 &= e^{-iHt} \rho e^{iHt} \\ \text{tr}(\rho_3 A), \quad \rho_3 &= e^{-iHt} B \rho B e^{iHt}. \end{aligned} \quad (21)$$

Therefore, in estimating (20), when  $n \leq \frac{1}{\epsilon^2}$ ,  $\mathcal{O}(\frac{n \log n}{\epsilon^2})$  samples suffice, and  $\mathcal{O}(\frac{\log n}{\epsilon^4})$  when  $n \geq \frac{1}{\epsilon^2}$ . Since there are  $n^2$  choices for  $k, l$ , the total sample complexity for estimating the correlation function (15) scales as  $\mathcal{O}(\frac{n^3 \log n}{\epsilon^2})$  when  $n \leq \frac{1}{\epsilon^2}$  and  $\mathcal{O}(\frac{n^2 \log n}{\epsilon^4})$  when  $n \geq \frac{1}{\epsilon^2}$ , respectively.  $\square$

---

**Protocol 1:** Fermionic-adapted shadow tomography 1 (FAST 1)

---

**Data:** Given initial state  $\rho$ , precision  $\epsilon > 0$

**Result:** approximate the correlation functions (15) for any  $i, j, k, l$

If  $n \leq \frac{1}{\epsilon^2}$ : **for**  $k, l = 1 : n$  **do**

Apply the protocol in Lemma 2 (if JW or BK mapping is applied) or in Lemma 3 (if TT is applied) for computing the quantities in (21)

Use the estimates of quantities to compute the correlation functions (9)

**end**

else:

**for**  $k, l = 1 : n$  **do**

Apply Lemma 4 for computing the quantities in (21)

Use the estimates of quantities to compute the correlation functions (9)

**end**

---

### Protocol for the anti-commutator case

We turn to the anti-commutator case. In this case, the important correlation function is the retarded Green's function (RGF),

$$G_{ab}^R(t) := -i\Theta(t) \text{tr}\left(\rho\{c_i(t), c_j^\dagger\}\right), \quad (22)$$

where  $c_i(t) := e^{iHt}c_i e^{-iHt}$  and  $\rho$  is the ground state of a quantum system. For a fixed time point  $t$ , we present a protocol that estimates the RGF's  $\{G_{ab}^R(t)\}_{a,b=1}^n$  to additive error  $\epsilon$ . Similar to Protocol 1, we consider the two regimes:  $n \leq \frac{1}{\epsilon^2}$  and  $n \geq \frac{1}{\epsilon^2}$ .

We first consider the regime where  $n \leq \frac{1}{\epsilon^2}$ . In this regime, we can estimate the Green's function without controlled time evolution. When JW or BK mapping is applied, we use the majority rule in Lemma 1 with the identities (12) and (13), with the circuit in Fig. 1c. Then, we estimate (22) for each pair  $(i, j)$ . Thus, the sample complexity and the number of measurement circuits remain comparable to brute-force measurements, scaling as  $\mathcal{O}(n^2)$ . If the TT mapping is used, the approach in Lemma 3 for the commutator case can be reused with the identities (12) and (13) based on Lemma 1. This approach reduces the number of measurement circuits by an order of magnitude with respect to system size. In Protocol 2, we outline this procedure as a conditional result.

In what follows, we propose two sample-efficient measurement strategies in the regime where  $n \geq \frac{1}{\epsilon^2}$ . When BK is used and  $n \geq \frac{1}{\epsilon^2}$ , we derive a measurement strategy from [23, Lemma 2.1] as follows

**Lemma 5.** *Assume that  $n \geq \frac{1}{\epsilon^2}$  and BK or TT mapping is applied. Then, there exists a shadow tomography protocol that uses  $\mathcal{O}\left(\frac{\log(\frac{1}{\epsilon})}{\epsilon^4}\right)$  single-copy and  $\mathcal{O}\left(\frac{\log(n)}{\epsilon^4}\right)$  two-copy measurements, and estimates the Majorana operators to additive error  $\epsilon$ , with  $\mathcal{O}\left(\frac{\log n}{\epsilon^4}\right)$  sample complexity and  $\mathcal{O}\left(\frac{1}{\epsilon^2}\right)$  circuits of  $\mathcal{O}(1)$  measurement circuit depth.*

*Proof.* Note that the  $2n$  Majorana operators mutually anti-commute. Thus, according to [23, Lemma 2.1], there are at most  $\mathcal{O}\left(\frac{1}{\epsilon^2}\right)$  observables whose expectation values are larger than  $\epsilon$ . Thus, we first apply the Bell sampling to threshold observables of small magnitudes and perform brute force measurements on the remaining observables. The first step requires two-copy measurements with  $\mathcal{O}\left(\frac{\log n}{\epsilon^4}\right)$  sample complexity and the other requires  $\mathcal{O}\left(\frac{1}{\epsilon^2} \cdot \frac{\log(\frac{1}{\epsilon})}{\epsilon^2}\right)$  single-copy brute force measurements. Since  $n \geq \frac{1}{\epsilon^2}$ , the sample complexity is  $\mathcal{O}\left(\frac{\log n}{\epsilon^4}\right)$ . Note that due to the brute force measurement, this procedure requires  $\mathcal{O}\left(\frac{1}{\epsilon^2}\right)$  circuits.  $\square$

We remark that the procedure shown in Lemma 5 can be directly applied for the case when JW mapping is applied. However, in the following section, we propose a measurement strategy specifically tailored to the JW mapping such that the number of circuits can be reduced from  $\mathcal{O}\left(\frac{1}{\epsilon^2}\right)$  in Lemma 5 to  $\mathcal{O}(1)$  and only  $\mathcal{O}(1)$  single-copy measurements suffice, which is a significant improvement.

When the JW mapping is applied and  $n \geq \frac{1}{\epsilon^2}$ , we can design a more efficient measurement strategy in terms of the number of circuits and , compared to the strategy in Lemma 5. In essence, our approach is divided into three steps as follows,

1. Estimate the magnitudes of Majorana operators under the JW mapping using the Bell sampling [58]
2. Throw away negligible observables and consider the remaining observables

3. Use a chained measurement strategy to determine the signs of the remaining observables.

The first two steps are typical in shadow tomography techniques based on Bell sampling [23, 58]. In the first step, we consider the following Pauli observables,

$$\{X_1, Z_1 X_2, \dots, Z_1 \cdots Z_{n-1} X_n, Y_1, Z_1 Y_2, \dots, Z_1 \cdots Z_{n-1} Y_n\}, \quad (23)$$

which correspond to the Majorana operators under the JW mapping. Notice that these observables mutually anticommute. Denoting this set of observables by  $\{P_i\}_{i=1}^{2n}$ , we apply the known Bell sampling procedure [23, 58] to the set  $\{P_i \otimes P_i\}_{i=1}^{2n}$ , and in the second step, neglect the observables that are estimated to have magnitudes less than  $\frac{3\epsilon}{4}$ .

For the last step, we introduce a variant of the Bell sampling strategy with more technical detail below Lemma 9. Here we provide a brief intuition behind the strategy. In the known Bell sampling strategy, we construct the mutually-commuting observables  $\{P_i \otimes P_i\}_{i=1}^{2n}$ . Instead of this, we consider the following construction of observables,

$$P_1 \otimes P_2, P_2 \otimes P_3, \dots, P_{2n-1} \otimes P_{2n}. \quad (24)$$

Notice that these observables mutually commute, since  $P_j$ 's mutually anticommute. Thus, we can estimate these observables simultaneously. With this in mind, if we estimate the sign of  $P_1$ , then we can infer that of  $P_2$  from the estimation of  $P_1 \otimes P_2$ , that of  $P_3$  from  $P_2 \otimes P_3$ , and so on. We call this a chained measurement strategy. Below Lemma 9, we discuss more detail for how to perform this chained measurement strategy. We here present a result for the proposed strategy as follows.

**Lemma 6.** *Assume that  $n \geq \frac{1}{\epsilon^2}$  and the JW mapping is applied. Then, there exists a shadow tomography protocol that uses  $\mathcal{O}(1)$  single-copy and  $\mathcal{O}(\frac{\log n}{\epsilon^4})$  two-copy measurements, and estimates the Majorana operators to additive error  $\epsilon$ , with  $\mathcal{O}(\frac{\log n}{\epsilon^4})$  sample complexity and  $\mathcal{O}(1)$  circuits of  $\mathcal{O}(1)$  measurement circuit depth.*

The proof of this lemma is shown below the proof of Lemma 9. To put together, we obtain the following theorem that states the overall complexity of a protocol for estimating the RGF (22).

**Theorem 2.** *There exists a shadow tomography protocol that uses at most two-copy measurements, and estimates the RGF (22) to additive error  $\epsilon$  with the following regimes:*

- if  $n \leq \frac{1}{\epsilon^2}$ , no sample complexity improvement over the brute force measurement but only the number of circuits is improved as  $\mathcal{O}(n)$  under TT mapping
- if  $n \geq \frac{1}{\epsilon^2}$ , the sample complexity scales as  $\mathcal{O}(\frac{n \log n}{\epsilon^4})$  under JW, BK, and TT mapping. In particular,  $\mathcal{O}(\frac{n}{\epsilon^2})$  circuits are required for the cases of BK and TT, and  $\mathcal{O}(n)$  circuits for JW.

*Proof.* Similar to the proof of Theorem 1, we fix  $j$  in (22) and consider the form of a sum of Pauli strings like (7). Then, estimating (22) reduces to computing

$$\text{tr}(\rho \{e^{iHt} c_j e^{-iHt}, B\}) \quad (25)$$

for a Pauli string  $B$  from  $c_j^\dagger$ . By Lemma 1, we use either of the identities (12) and (13) depending on the measurement outcomes, and then apply Lemma 3 for the case where  $n \leq \frac{1}{\epsilon^2}$  and TT is applied, Lemma 5 for the case where  $n \geq \frac{1}{\epsilon^2}$  and BK or TT is applied, and Lemma 6 for the case where  $n \geq \frac{1}{\epsilon^2}$  and JW is applied. Since there are  $n$  choices for the index  $j$ , the total sample complexity and the number of measurement circuits required for each of the three cases can be derived as in the statement.  $\square$

---

**Protocol 2:** Fermionic-adapted shadow tomography 2 (FAST 2: conditional anti-commutator protocol)

---

**Data:** Given initial state  $\rho$ , precision  $\epsilon > 0$

**Result:** approximate the RGF (22) for any  $a, b$  (**with sample-efficiency gains only in the regime  $n \geq \frac{1}{\epsilon^2}$** )

If  $n \leq \frac{1}{\epsilon^2}$ :

**for**  $b = 1 : n$  **do**

Perform the brute force measurement strategy if JW or BK mapping is applied, with the circuit in Fig. 1c.

Apply the method in Lemma 3 when TT is applied, with the circuit in Fig. 1d.

Use the resulting measurement outcomes to compute the RGFs by selecting either of the representations (12) or (13).

**end**

else:

**for**  $b = 1 : n$  **do**

Apply Lemma 6 (if JW mapping is applied) or Lemma 5 (if BK or TT is used)

Use the resulting measurement outcomes to compute the RGFs by selecting either of the representations (12) or (13).

**end**

---

Again we remark that unlike the commutator case in Protocol 1, there needs an additional step of selecting either of the representations (12) or (13) in Protocol 2. However, this additional step is performed without any further quantum simulations, by doing classical post-processing on the measurement results. Specifically, as discussed above Lemma 1, we count the number of  $|0\rangle$  and  $|1\rangle$  states in the ancilla qubit and know whether  $\rho_+$  in (12) appears more than  $\rho_-$  in (13) or vice versa. By this majority rule, we select either of the representations (12) or (13).

### Complexity tables for the proposed protocols and brute force measurements

We summarize the overall complexity for Protocol 1 and Protocol 2 in Table IV and Table V, respectively. On the other hand, Table VI shows the overall complexity for brute force measurements.

#### A. Numerical result

We validate Protocol 1 for the estimation of bosonic correlation functions (15) with numerical simulations. We focus on the regime  $n \leq \frac{1}{\epsilon^2}$ , which is of practical interest as will be shown in Corollary 1. We compare our protocol in Lemma 3 with the typical brute force strategy that estimates the values of the form  $\text{tr}(\rho[e^{iHt}\gamma_i\gamma_j e^{-iHt}, \gamma_k\gamma_l])$  via a Hadamard test. That is, controlled Pauli operations for the Pauli strings corresponding to the products of Majorana operators,  $\gamma_i\gamma_j$  and  $\gamma_k\gamma_l$ , are implemented, as the setting in Table II with the circuits [11]. The resulting correlation values can be used to estimate the correlation functions in (15).

We use the TT mapping for the two approaches. For demonstration purposes, we study a one-dimensional toy model with periodic boundary condition (i.e.  $c_{n+1} = c_1$ ), known as the

Correlation functions	Commutator		Anti-commutator	
	$n \leq \frac{1}{\epsilon^2}$	$n \geq \frac{1}{\epsilon^2}$	$n \leq \frac{1}{\epsilon^2}$	$n \geq \frac{1}{\epsilon^2}$
Sample complexity	$\mathcal{O}(\frac{n^3 \log n}{\epsilon^2})$	$\mathcal{O}(\frac{n^2 \log n}{\epsilon^4})$	$\mathcal{O}(\frac{n^2 \log n}{\epsilon^2})^a$	$\mathcal{O}(\frac{n \log n}{\epsilon^4})$
Qubit count <sup>b</sup>	$n$	$2n$	$n + 1$	$2n + 2$
Ancilla qubit	0	0	1	2
Copy count	1	2	1	2

<sup>a</sup> No improvement over the brute force strategy of measurement

<sup>b</sup> For the case of TT mapping, the number of qubits equal to the system size when  $n = \frac{3^h - 1}{2}$  for tree height  $h \geq 1$ , otherwise it is generally larger but at most  $2n$  [57].

TABLE IV: Summary of Protocol 1 and Protocol 2 for estimating the correlation functions (15) and (22) in terms of sample complexity, the number of qubits required (Qubit count), the number of ancilla qubits (Ancilla qubit), and the maximal number of copies of the initial quantum state used (Copy count).

Correlation functions	Commutator			Anti-commutator			
	$n \leq \frac{1}{\epsilon^2}$	$n \leq \frac{1}{\epsilon^2}$	$n \geq \frac{1}{\epsilon^2}$	$n \leq \frac{1}{\epsilon^2}$	$n \leq \frac{1}{\epsilon^2}$	$n \geq \frac{1}{\epsilon^2}$	$n \geq \frac{1}{\epsilon^2}$
Mapping	JW,BK	TT	JW,BK,TT	JW, BK	TT	BK, TT	JW
Measurement	MMC	DC	B + MMC	BM	DC	B + BM	B + BM
Circuit construction time	$\mathcal{O}(n^6)$	$\mathcal{O}(n^2)$	$\mathcal{O}(\frac{n^5}{\epsilon^2})$	$\mathcal{O}(n^2)$	$\mathcal{O}(n)$	$\mathcal{O}(\frac{n}{\epsilon^2})$	$\mathcal{O}(n)$
Circuit depth	$\mathcal{O}(n)$	$\mathcal{O}(1)$	$\mathcal{O}(n)$	$\mathcal{O}(1)$	$\mathcal{O}(1)$	$\mathcal{O}(1)$	$\mathcal{O}(1)$
Circuit count	$\mathcal{O}(n^3)$	$\mathcal{O}(n^2)$	$\mathcal{O}(\frac{n^2}{\epsilon^2})$	$\mathcal{O}(n^2)$	$\mathcal{O}(n)$	$\mathcal{O}(\frac{n}{\epsilon^2})$	$\mathcal{O}(n)$
Circuit	Fig. 1a	Fig. 1b	Fig. 1a, Fig. 1e	Fig. 1c	Fig. 1d	Fig. 1c, Fig. 1f	Fig. 1c, Fig. 1f
Result	Lemma 2	Lemma 3	Lemma 4	-	Lemma 3	Lemma 5	Lemma 6

TABLE V: Summary of Protocol 1 and Protocol 2 for estimating the correlation functions (15) and (22) in terms of the fermion-to-qubit mapping (Mapping), the types of measurements (Measurement), classical time for constructing measurement circuits (Circuit construction time), the circuit depth required for the corresponding measurements (Circuit depth), the number of circuits to execute (Circuit count), circuit structure used for execution (Circuit), and the corresponding lemma (Result). The measurement types are abbreviated as follows: Clifford measurements for mutually commuting observables (MMC), random Pauli measurements combined with dynamic circuits (DC), Bell sampling (B), and brute force measurements in the computational basis (BM). As discussed in [23], techniques in the stabilizer formalism [59] can be used to construct a Clifford circuit for MMC within  $\mathcal{O}(n^3)$  time. Therefore, in the cases where MMC is considered, the time complexity is estimated as  $\mathcal{O}(n^3) \times$  Circuit count, since MMC is performed independently for each circuit in the protocols.

Su–Schrieffer–Heeger (SSH) model,

$$H = -V_{nn} \sum_{i=1}^n (1 + (-1)^i \frac{\delta}{2}) [c_i^\dagger c_{i+1} + c_{i+1}^\dagger c_i] - \mu \sum_{i=1}^n c_i^\dagger c_i. \quad (26)$$

Here, we set  $V_{nn} = 1$  and  $\delta = 0.4$ . In addition, with respect to system size  $n$ , we adjust  $\mu$  such that

Correlation functions	Commutator	Anti-commutator
Sample complexity	$\mathcal{O}(\frac{n^4 \log n}{\epsilon^2})$	$\mathcal{O}(\frac{n^2 \log n}{\epsilon^2})$
Qubit count <sup>a</sup>	$n$	$n + 1$
Ancilla qubit	0	1
Time complexity	$\mathcal{O}(1)$	$\mathcal{O}(1)$
Circuit depth	$\mathcal{O}(1)$	$\mathcal{O}(1)$
Circuit count	$\mathcal{O}(n^4)$	$\mathcal{O}(n^2)$
Circuit	Fig. 1a	Fig. 1c

<sup>a</sup> For the case of TT mapping, the number of qubits equal to the system size when  $n = \frac{3^h - 1}{2}$  for tree height  $h \geq 1$ , otherwise it is generally larger but at most  $2n$  [57].

TABLE VI: Summary of brute force measurements for computing the correlation functions (15) and (22). These approaches require only single-copy measurements.

the zero momentum state becomes the ground state of the Hamiltonian

$$|\psi_{GS}\rangle = \frac{1}{\sqrt{n}} \sum_{j=1}^n c_j^\dagger |0\rangle. \quad (27)$$

For our simulations, we implement a Pauli algebra backend that leverages symbolic dictionary representations for the efficient construction and manipulation of fermionic operators. To execute the classical shadow sampling, we compute the exact statevectors and accelerate the measurement process by distributing the required shots across parallelized routines. For the brute-force measurements, we emulate the Hadamard tests with Bernoulli random variables whose expectation values correspond to given unitary observables.

Fig. 2 illustrates the scaling of the maximum of errors between exact and estimated correlation functions with respect to system size, which is defined by

$$\max_{i,j \in [n]} |f_{ij} - \tilde{f}_{ij}|, \quad f_{ij} = \text{tr} \left( \rho \{ e^{iHt} c_i^\dagger c_j e^{-iHt}, c_a^\dagger c_b \} \right). \quad (28)$$

Here  $\tilde{f}_{ij}$  represents the estimated expectation value and the indices,  $a, b \in [n]$ , are fixed. We set  $t = 1$  for the simulations in Fig. 2.

Regarding the shot cost, we fix total measurement budgets such that  $N_{\text{FAST}} = 3N_{\text{brute-force}} = 80000$ , which denote the total number of shots for the FAST and brute-force measurements in each of the simulation results in Fig. 2. With this setting, we can make the variance of estimates obtained from the two methods comparable in estimating the correlation function,  $\text{tr}(\rho[e^{iHt} \gamma_i \gamma_j e^{-iHt}, \gamma_k \gamma_l])$ . One reason is that the variance for brute-force measurements with Hadamard tests is no greater than 1, while the FAST involves a sum of three variances of independent classical shadows, due to the identity (9). With the fixed total shot numbers, we distribute them across the required measurement circuits. For the case of brute-force measurements, we require a measurement circuit for each combination  $(i, j, k, l)$ . Here the number of pairs  $(k, l)$  is either 1 or 4, since the two indices correspond to a fixed one-body observable in (28). In contrast, the FAST requires only either 3 or 12 circuits for measurements, according to Lemma 3. Additionally, the FAST does not require controlled Pauli operations, while the brute-force measurements do. This is summarized in Table VII.

We perform 10 independent simulations for each system size  $n$ , plotting the resulting mean maximum error and its standard deviation in Fig. 2. Given the fixed shot number, the error estimate,  $\max_{i,j} |f_{ij} - \tilde{f}_{ij}|$ , increases with system size. Importantly, Lemma 3 implies that the error within our protocol scales as  $\mathcal{O}(\sqrt{n \log n})$ , while the error for brute-force measurements scales as  $\mathcal{O}(n\sqrt{\log n})$ . We can clearly see this quantitative divergence in Fig. 2, by observing that the error occurring from brute-force measurements grows much faster than our method. From this observation, we expect that for large systems, the FAST would outperform brute-force measurements.

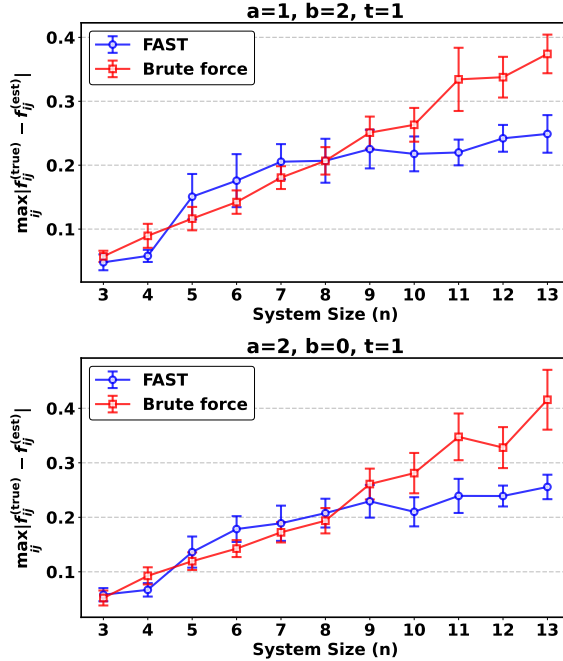


FIG. 2: Simulation results that show the maximum of errors between exact and estimated correlation functions of the form in (28), which are obtained from the FAST and brute-force measurements. The parameters  $(a, b)$  are set to  $(1, 2)$  and  $(2, 2)$  for the top and bottom panels, respectively. The y-axis indicates the maximum error between exact and estimated correlation functions.

## DISCUSSION

In this work, we present a framework for estimating the dynamical correlation functions using shadow tomography techniques. We introduce Fermionic-Adapted Shadow Tomography (FAST) protocols (Protocol 1 and Protocol 2), for efficiently estimating the commutator and anti-commutator correlation functions, respectively. The connection is established by reformulating these functions in a form amenable to direct measurement, thereby enabling their estimation

Method	FAST	Brute force
The number of measurement circuits	$3n_{ab}$	$4n_{ab}n^2$
Controlled Pauli operation	No	Yes
Ancilla qubit	0	1

TABLE VII: Comparison of our method (FAST) with a brute-force strategy of measurements for the simulations in Fig. 2. The  $n_{ab}$  indicates the number of Majorana operators that form the 1-body observable  $c_a^\dagger c_b$ . If  $a = b$ ,  $n_{ab} = 1$ , otherwise  $n_{ab} = 4$ .

via shadow tomography techniques. We expect the proposed protocols to be broadly applicable to practical problems in quantum simulation of many-body systems.

We remark that from the commutator representation (9), and the anti-commutator ones in (12) and (13), we can straightforwardly estimate the general form of the correlation functions (1) by summing them up,  $\text{tr}(\rho A(t)B)$  where  $A$  and  $B$  correspond to 1-body fermionic observables. In that process, we will use the measurement strategies in Protocol 1 only, since they target 1-body fermionic observables. Therefore, we can extend our protocol to sample-efficient estimation for two-particle correlation functions of the form,  $\text{tr}(\rho c_i(t)^\dagger c_j(t) c_k(0)^\dagger c_l(0))$ , and the sample-complexity improvement would follow from Protocol 1. We formally state this as in the following corollary,

**Corollary 1.** *Estimating the density-density response function (6) to additive error  $\epsilon$  requires  $\mathcal{O}\left(\frac{n^3 \log n}{\epsilon^2}\right)$  sample complexity using Protocol 1 with  $\mathcal{O}(n^3)$  circuits (JW, BK) or  $\mathcal{O}(n^2)$  circuits (TT), while the brute force measurement demands  $\mathcal{O}\left(\frac{n^4 \log n}{\epsilon^2}\right)$  with  $\mathcal{O}(n^4)$  circuits.*

As a potential application of Protocol 2, we may consider the estimation of the retarded Green's function in momentum space. To illustrate this, for the system with one fermionic mode at each lattice site, the single-particle Green's functions in the momentum space is given by

$$G_{k,\sigma}^R(t) = \frac{1}{n} \sum_{a,b=1}^n G_{ab,\sigma}^R(t) e^{-ik(a-b)}. \quad (29)$$

To estimate  $G_{k,\sigma}^R(t)$  within a target tolerance  $\epsilon_{\text{tol}}$ , each entry  $G_{ab,\sigma}^R(t)$  must be computed to precision  $\epsilon = \frac{\epsilon_{\text{tol}}}{n}$  by the Gershgorin circle theorem in the worst-case scenario. This places the problem in the regime  $n \leq \frac{1}{\epsilon^2}$  of Protocol 2, where our protocol does not improve sample complexity but reduce the number of measurement circuits by an order of magnitude with respect to system size. However, we anticipate no general improvement in sample complexity for estimating Green's functions. This limitation arises from the mutual anti-commutation relations of Majorana operators, a point also noted by Kökcü et al. [14].

## METHODS

### The triply efficient shadow tomography for learning 1-body observables

In this section, we review on a specialized application of the shadow tomography protocol by King *et al* [23], in order to derive the result in Lemma 4.

**Lemma 7.** [23, Lemma 1.1] *The size of the largest clique in  $G_\epsilon$  is at most  $\frac{4}{\epsilon^2}$  with high probability.*

**Lemma 8.** [23, Lemma 4.1] *Let  $G'$  be a subgraph of the commutation graph of  $G(\mathcal{F}_1^{(n)})$  of 1-body observables, and  $\omega$  is the size of the largest clique in  $G'$ . Then, there is a classical algorithm that outputs a coloring of  $G'$  with  $\mathcal{O}(n^2\omega)$  runtime using at most  $\omega + 1$  colors.*

Using these lemmas, we prove Lemma 4, which follows from the original work [23].

*Proof.* Let  $G_\epsilon$  be the subgraph of the commutation graph for the 1-body observables after thresholding observables of magnitudes less than  $\epsilon$ .

By Lemma 7 and Lemma 8, coloring  $G_\epsilon$  requires  $\frac{4}{\epsilon^2} + 1$  colors, and for each color, there are at most  $\mathcal{O}(n^2)$  observables, since the number of 1-body observables is  $\mathcal{O}(n^2)$ . This means that measuring the observables for each color requires  $\mathcal{O}(\frac{\log \frac{n}{\delta}}{\epsilon^2})$  sample complexity using Clifford measurements [59]. Since there are  $\mathcal{O}(\frac{1}{\epsilon^2})$  colors, the total sample complexity is  $\mathcal{O}(\frac{\log \frac{n}{\delta}}{\epsilon^4})$ . Since the number of 1-body observables scales as  $\mathcal{O}(n^2)$ , by setting the new failure probability as  $\delta \leftarrow \frac{\delta}{n^2}$ , we can learn the observables in  $G_\epsilon$  with probability at least  $1 - \delta$  using  $\mathcal{O}(\frac{\log n}{\epsilon^4})$  samples, and  $\mathcal{O}(\frac{1}{\epsilon^2})$  circuits corresponding to the colors. Therefore, measuring all observables in  $G_\epsilon$  with single-copy measurements can be done with  $\mathcal{O}(\frac{\log n}{\epsilon^4})$  sample complexity and  $\mathcal{O}(\frac{1}{\epsilon^2})$  Clifford measurement circuits.  $\square$

### Probabilistic state preparation based on measurements

Within the circuit Fig. 1c, the state is evolved as follows,

$$\begin{aligned}
& |0\rangle\langle 0| \otimes \rho \\
& \rightarrow |+\rangle\langle +| \otimes \rho \\
& \rightarrow |0\rangle\langle 0| \otimes \rho + |1\rangle\langle 0| \otimes B\rho + |0\rangle\langle 1| \otimes \rho B + |1\rangle\langle 1| \otimes B\rho B \\
& \rightarrow |0\rangle\langle 0| \otimes e^{iHt} \rho e^{-iHt} + |1\rangle\langle 0| \otimes e^{iHt} B \rho e^{-iHt} + |0\rangle\langle 1| \otimes e^{iHt} \rho B e^{-iHt} + |1\rangle\langle 1| \otimes e^{iHt} B \rho B e^{-iHt} \\
& \rightarrow |+\rangle\langle +| \otimes e^{iHt} \rho e^{-iHt} + |-\rangle\langle +| \otimes e^{iHt} B \rho e^{-iHt} + |+\rangle\langle -| \otimes e^{iHt} \rho B e^{-iHt} + |-\rangle\langle -| \otimes e^{iHt} B \rho B e^{-iHt} \\
& \implies \rho_+ \text{ if 0 in the ancilla with probability } C_+^2, \rho_- \text{ if 1 in the ancilla with probability } C_-^2,
\end{aligned} \tag{30}$$

where  $\rho_\pm$  and  $C_\pm$  are defined in (12) and (13). Similarly, we can obtain states  $\rho_\pm$  within the circuits Fig. 1d, and Fig. 1f.

### Chained measurement strategy for the JW-mapped Majorana operators

In this section, we prove Lemma 6. To proceed, we first consider the following preliminary exercise.

For the independent events that  $C = 1$  and  $D = 1$ , we let  $\mathbb{P}(C = 1) \geq 1 - \delta_1$  and  $\mathbb{P}(D = 1) \geq 1 - \delta_2$ . Then, we have

$$\mathbb{P}(CD = 1) \geq \mathbb{P}(C = 1, D = 1) = \mathbb{P}(C = 1)\mathbb{P}(D = 1) \geq (1 - \delta_1)(1 - \delta_2). \tag{31}$$

This implies that if random variables,  $\hat{a}$  and  $\hat{b}$ , satisfy that  $\text{sign}(\hat{a}) = \text{sign}(a)$  and  $\text{sign}(\hat{b}) = \text{sign}(b)$  with high probability for the corresponding true values,  $a$  and  $b$ , then  $\text{sign}(\hat{a}\hat{b}) = \text{sign}(ab)$  with h.p. This can be understood by setting  $C = \text{sign}(\hat{a})\text{sign}(a)$  and  $D = \text{sign}(\hat{b})\text{sign}(b)$ .

The RGF calculations in (22) consider the annihilation and creation observables, which are represented by the Majorana operators under the JW mapping

$$S_X := \{X_1, Z_1 X_2, \dots, Z_1 \cdots Z_{n-1} X_n\}, \quad S_Y := \{Y_1, Z_1 Y_2, \dots, Z_1 \cdots Z_{n-1} Y_n\}. \quad (32)$$

For convenience, we denote  $\{P_i\}_{i=1}^n$  and  $\{Q_i\}_{i=1}^n$  to be the sets  $S_X$  and  $S_Y$ . The indices are arranged consistently with the elements of the sets. For example,  $P_1 = X_1$ ,  $P_3 = Z_1 Z_2 X_3$ ,  $Q_n = Z_1 \cdots Z_{n-1} Y_n$ , and so forth. Notice that the observables in both sets mutually anticommute. In this case, the use of the coloring strategy [23] does not give any efficiency for the problem here, since any subset of the Majorana observables consists of mutually anticommuting Paulis.

Here we introduce a novel shadow tomography protocol based on Bell sampling. Our protocol is tailored to the set of Majorana observables in (32). Suppose that the Bell sampling for neglecting observables of small magnitudes is already performed [23, 58]. We let  $\{P_{r_i}\}_{i=1}^I$  and  $\{Q_{k_j}\}_{j=1}^J$  be the remaining observables as subsets of  $S_X$  and  $S_Y$ , respectively, where  $r_i$ 's and  $k_j$ 's are arranged in increasing order. We define the two sets of observables as follows,

$$B_X := \{P_{r_i} \otimes P_{r_{i+1}} : i \in [I-1]\}, \quad B_Y := \{Q_{k_j} \otimes Q_{k_{j+1}} : j \in [J-1]\}. \quad (33)$$

In the following, we show that a property of the two sets (33),

**Lemma 9.** *The Pauli strings in  $B_X$  mutually commute with the common eigenstates as follows,*

$$\{ |Bell\rangle_{r_1, n+r_2} |Bell\rangle_{r_2, n+r_3} \cdots |Bell\rangle_{r_{I-1}, n+r_I} |b\rangle : b \text{ is the computational basis on the remaining qubits} \}, \quad (34)$$

where  $|Bell\rangle_{a,b}$  denotes the four possible Bell states acting on qubit  $a$  and qubit  $b$ . Similarly, the Pauli strings in  $B_Y$  have eigenstates as

$$\{ |Bell\rangle_{k_1, n+k_2} |Bell\rangle_{k_2, n+k_3} \cdots |Bell\rangle_{k_{J-1}, n+k_J} |b\rangle : b \text{ is the computational basis on the remaining qubits} \}. \quad (35)$$

*Proof.* We prove the statement by induction on the cardinality of set  $B_X$ . For  $I = 3$ , it is trivial. Suppose the statement holds up to  $I \leq \mathfrak{J}$ . We consider the case  $I = \mathfrak{J} + 1$ . Using the hypothesis for the subset of  $B_X$ , which consists of the first  $\mathfrak{J}$  elements of  $B_X$ , we know that

$$|Bell\rangle_{r_1, n+r_2} |Bell\rangle_{r_2, n+r_3} \cdots |Bell\rangle_{r_{\mathfrak{J}-1}, n+r_{\mathfrak{J}}} |b\rangle \quad (36)$$

forms the common eigenstate basis for the observables in the subset of  $B_X$ . Here, in the computational basis state  $|b\rangle$ , we can define the bell states that act on qubit  $r_{\mathfrak{J}}$  and qubit  $n+r_{\mathfrak{J}+1}$ . That is, the common eigenstate basis mentioned above can be changed into

$$|Bell\rangle_{r_1, n+r_2} |Bell\rangle_{r_2, n+r_3} \cdots |Bell\rangle_{r_{\mathfrak{J}-1}, n+r_{\mathfrak{J}}} |Bell\rangle_{r_{\mathfrak{J}}, n+r_{\mathfrak{J}+1}} |b\rangle. \quad (37)$$

This eigenstate is still shared by the subset of  $B_X$  mentioned above. Now, it suffices to check whether this state is an eigenstate for the last observable  $P_{r_{\mathfrak{J}}} \otimes P_{r_{\mathfrak{J}+1}}$ . In fact, this is trivial by noticing that for the bell states  $\{|Bell\rangle_{r_j, n+r_{j+1}}\}_{j=1}^{\mathfrak{J}-1}$ , they are transformed by the Pauli operator  $Z \otimes Z$  in  $P_{r_{\mathfrak{J}}} \otimes P_{r_{\mathfrak{J}+1}}$  and the last state  $|Bell\rangle_{r_{\mathfrak{J}}, n+r_{\mathfrak{J}+1}}$  by the operator  $X \otimes X$  in  $P_{r_{\mathfrak{J}}} \otimes P_{r_{\mathfrak{J}+1}}$ . Therefore, this completes the proof.  $\square$

Now we prove Lemma 6 using Lemma 9.

*Proof.* For a given state  $\rho$ , our goal is to estimate the Majorana observables in (32), that is,  $\text{tr}(\rho O)$  for each  $O \in S_X \cup S_Y$ . We perform single-copy measurements and two-copy measurements as follows,

1. Estimate the magnitudes of expectations of observables in (32) to precision  $\epsilon$   
(Two-copy measurements with  $\mathcal{O}(\frac{\log n}{\epsilon^4})$  sample complexity)
2. Throw away observables having small magnitudes ( $\leq \frac{3\epsilon}{4}$ ).  
( $\mathcal{O}(n)$  classical time)
3. Let us consider the remaining observables, denoted as  $\{P_{r_i}\}_{i=1}^I$  and  $\{Q_{k_j}\}_{j=1}^J$  in (33).
4. Measure the first observables,  $P_{r_1}, Q_{k_1}$ , to precision  $\epsilon^2$ ,  $\text{tr}(\rho P_{r_1})$  and  $\text{tr}(\rho Q_{k_1})$ .  
(Single-copy measurements with  $\mathcal{O}(\frac{1}{\epsilon^2})$  sample complexity)
5. Measure the observables in (33) to precision  $\epsilon^2$  using the measurement basis in Lemma 9.  
(Two-copy measurements with  $\mathcal{O}(\frac{\log \min\{n, \max\{I, J\}\}}{\epsilon^4})$  sample complexity, where  $I, J \leq n$ . Note that particularly when  $n \geq \frac{1}{\epsilon^2}$ , according to [23, Lemma 2.1],  $\max\{I, J\} = \mathcal{O}(\frac{1}{\epsilon^2})$ .)

In total, our protocol incurs  $\mathcal{O}(\frac{\log n}{\epsilon^4})$  sample complexity and  $\mathcal{O}(n)$  classical time cost, and  $\mathcal{O}(1)$  circuits.

From the data analysis point of view, we perform three independent experiments (i.e. step 1, step 4, step 5 in the above protocol). The first experiment gives us the estimates of magnitudes,  $\{p_{r_i}^{(1)}\}, \{q_{k_j}^{(1)}\}$  with probability at least  $1 - \delta_1$

$$|\text{tr}(\rho P_{r_i})|, |\text{tr}(\rho Q_{k_j})| \geq \frac{\epsilon}{2}, \left| p_{r_i}^{(1)} - |\text{tr}(\rho P_{r_i})| \right| \leq \frac{\epsilon}{4}, \left| q_{k_j}^{(1)} - |\text{tr}(\rho Q_{k_j})| \right| \leq \frac{\epsilon}{4}, \quad (38)$$

the second experiment produces the estimates of the first observables,  $p_{r_1}^{(2)}, q_{k_1}^{(2)}$ , with probability at least  $1 - \delta_2$

$$\left| p_{r_1}^{(2)} - \text{tr}(\rho P_{r_1}) \right| \leq \frac{\epsilon}{4}, \left| q_{k_1}^{(2)} - \text{tr}(\rho Q_{k_1}) \right| \leq \frac{\epsilon}{4}, \quad (39)$$

and the last gives the estimates of the chained trace multiplications,  $\{p_{r_i}^{(3)}\}, \{q_{k_j}^{(3)}\}$ , with probability at least  $1 - \delta_3$

$$\left| p_{r_i, r_{i+1}}^{(3)} - \text{tr}(\rho P_{r_i}) \text{tr}(\rho P_{r_{i+1}}) \right| \leq \frac{\epsilon^2}{8}, \left| q_{k_j, k_{j+1}}^{(3)} - \text{tr}(\rho Q_{k_j}) \text{tr}(\rho Q_{k_{j+1}}) \right| \leq \frac{\epsilon^2}{8}. \quad (40)$$

Since the events in (38), (39), (40) happens independently. the above inequalities hold simultaneously with probability at least  $(1 - \delta_1)(1 - \delta_2)(1 - \delta_3)$ .

We claim that from the inequalities, we can estimate the Majorana observables in (32). From (38), we estimate the magnitudes of expectation values of observables, and consider only the observables of magnitudes no less than  $\frac{3\epsilon}{4}$ . From (39), we estimate the signs of the first expectation values.

With (38) and (40), we know that  $\{p_{r_i}^{(3)}\}, \{q_{k_j}^{(3)}\}$  have the same sign as the corresponding true values. For example, (38) implies that

$$|\mathrm{tr}(\rho P_{r_i}) \mathrm{tr}(\rho P_{r_{i+1}})| \geq \frac{\epsilon^2}{4}, \quad (41)$$

and from (40), we see that

$$\left| p_{r_i, r_{i+1}}^{(3)} - \mathrm{tr}(\rho P_{r_i}) \mathrm{tr}(\rho P_{r_{i+1}}) \right| \leq \frac{\epsilon^2}{8}. \quad (42)$$

Therefore, the signs of the estimate  $p_{r_i, r_{i+1}}^{(3)}$  and the corresponding true value  $\mathrm{tr}(\rho P_{r_i}) \mathrm{tr}(\rho P_{r_{i+1}})$  are the same. It is the same for the other estimates in (40). Together with (39) and (31), we estimate the signs of the estimates in (38) by tracking the sign of  $p_{r_1}^{(2)} p_{r_1, r_2}^{(3)}$ , that of  $p_{r_1}^{(2)} p_{r_1, r_2}^{(3)} p_{r_2, r_3}^{(3)}$ , and so forth. Therefore, we prove the claim and completes the proof of Lemma 6.  $\square$

### ACKNOWLEDGEMENTS

This research was supported by Quantum Simulator Development Project for Materials Innovation through the National Research Foundation of Korea (NRF) funded by the Korean government (Ministry of Science and ICT(MSIT))(No. NRF- 2023M3K5A1094813). SC was supported by a KIAS Individual Grant (CG090601) at Korea Institute for Advanced Study. TK is supported by a KIAS Individual Grant (CG096001) at Korea Institute for Advanced Study. M.H. is supported by a KIAS Individual Grant (No. CG091301) at Korea Institute for Advanced Study. We used resources of the Center for Advanced Computation at Korea Institute for Advanced Study and the National Energy Research Scientific Computing Center (NERSC), a U.S. Department of Energy Office of Science User Facility operated under Contract No.DE-AC02-05CH11231.

### CODE AVAILABILITY

Code used for the current study are available at the following GitHub repository:  
<https://github.com/TKmath/FAST-for-dynamical-correlation-functions>.

### DATA AVAILABILITY

All data that support the findings of this study are included within the Github repository in Code availability.

### DECLARATIONS

#### Author Contributions

TK conceptualized the idea and performed the theoretical and numerical analyses. TK and SC wrote the main manuscript. TK, MH, HP, and SC contributed to finalizing the manuscript.

## Competing Interests

The authors declare no competing financial or non-financial interests.

- 
- [1] Seth Lloyd. Universal quantum simulators. *Science*, 273(5278):1073–1078, 1996.
  - [2] Alán Aspuru-Guzik, Anthony D Dutoi, Peter J Love, and Martin Head-Gordon. Simulated quantum computation of molecular energies. *Science*, 309(5741):1704–1707, 2005.
  - [3] Hsin-Yuan Huang, Richard Kueng, and John Preskill. Predicting many properties of a quantum system from very few measurements. *Nature Physics*, 16(10):1050–1057, 2020.
  - [4] Bela Bauer, Sergey Bravyi, Mario Motta, and Garnet Kin-Lic Chan. Quantum algorithms for quantum chemistry and quantum materials science. *Chemical reviews*, 120(22):12685–12717, 2020.
  - [5] Gerald D Mahan. *Many-particle physics*. Springer Science & Business Media, 2013.
  - [6] Gordon Baym and Leo P. Kadanoff. Conservation Laws and Correlation Functions. 124(2):287–299.
  - [7] J. M. Luttinger and J. C. Ward. Ground-State Energy of a Many-Fermion System. II. 118(5):1417–1427.
  - [8] M. Potthoff. Self-energy-functional approach to systems of correlated electrons. 32(4):429–436.
  - [9] Suguru Endo, Iori Kurata, and Yuya O Nakagawa. Calculation of the green’s function on near-term quantum computers. *Physical Review Research*, 2(3):033281, 2020.
  - [10] Shota Kanasugi, Shoichiro Tsutsui, Yuya O Nakagawa, Kazunori Maruyama, Hiroataka Oshima, and Shintaro Sato. Computation of green’s function by local variational quantum compilation. *Physical Review Research*, 5(3):033070, 2023.
  - [11] Martin Mootz, Thomas Iadecola, and Yong-Xin Yao. Adaptive variational quantum computing approaches for green’s functions and nonlinear susceptibilities. *Journal of Chemical Theory and Computation*, 20(19):8689–8710, 2024.
  - [12] Niladri Gomes, David B Williams-Young, and Wibe A de Jong. Computing the many-body green’s function with adaptive variational quantum dynamics. *Journal of Chemical Theory and Computation*, 19(11):3313–3323, 2023.
  - [13] Hongxiang Chen, Max Nusspickel, Jules Tilly, and George H Booth. Variational quantum eigensolver for dynamic correlation functions. *Physical Review A*, 104(3):032405, 2021.
  - [14] Efehan Kökcü, Heba A Labib, JK Freericks, and Alexander F Kemper. A linear response framework for quantum simulation of bosonic and fermionic correlation functions. *Nature Communications*, 15(1):3881, 2024.
  - [15] Bela Bauer, Dave Wecker, Andrew J Millis, Matthew B Hastings, and Matthias Troyer. Hybrid quantum-classical approach to correlated materials. *Physical Review X*, 6(3):031045, 2016.
  - [16] Taichi Kosugi and Yu-ichiro Matsushita. Linear-response functions of molecules on a quantum computer: Charge and spin responses and optical absorption. *Physical Review Research*, 2(3):033043, 2020.
  - [17] Alessandro Chiesa, Francesco Tacchino, Michele Grossi, Paolo Santini, Ivano Tavernelli, Dario Gerace, and Stefano Carretta. Quantum hardware simulating four-dimensional inelastic neutron scattering. *Nature Physics*, 15(5):455–459, 2019.
  - [18] Mancheon Han, Hyowon Park, and Sangkook Choi. Quantum zeno monte carlo for computing observables. *npj Quantum Inf.*, 11(arXiv: 2403.02763):46, 2025.
  - [19] Yu Tong, Dong An, Nathan Wiebe, and Lin Lin. Fast inversion, preconditioned quantum linear system solvers, fast green’s-function computation, and fast evaluation of matrix functions. *Physical Review A*, 104(3):032422, 2021.
  - [20] Samuele Piccinelli, Francesco Tacchino, Ivano Tavernelli, and Giuseppe Carleo. Efficient calculation of green’s functions on quantum computers via simultaneous circuit perturbation. *arXiv preprint arXiv:2505.05563*, 2025.

- [21] William J Huggins, Kianna Wan, Jarrod McClean, Thomas E O'Brien, Nathan Wiebe, and Ryan Babbush. Nearly optimal quantum algorithm for estimating multiple expectation values. *Physical Review Letters*, 129(24):240501, 2022.
- [22] Pengfei Wang, Hyukjoon Kwon, Chun-Yang Luan, Wentao Chen, Mu Qiao, Zinan Zhou, Kaizhao Wang, MS Kim, and Kihwan Kim. Snapshotting quantum dynamics at multiple time points. *Nature Communications*, 15(1):8900, 2024.
- [23] Robbie King, David Gosset, Robin Kothari, and Ryan Babbush. Triply efficient shadow tomography. In *Proceedings of the 2025 Annual ACM-SIAM Symposium on Discrete Algorithms (SODA)*, pages 914–946. SIAM, 2025.
- [24] Reinis Irmejs and Raul A Santos. Approximating dynamical correlation functions with constant depth quantum circuits. *Quantum*, 9:1639, 2025.
- [25] Artur F Izmaylov, Tzu-Ching Yen, Robert A Lang, and Vladyslav Verteletskyi. Unitary partitioning approach to the measurement problem in the variational quantum eigensolver method. *Journal of chemical theory and computation*, 16(1):190–195, 2019.
- [26] Ikko Hamamura and Takashi Imamichi. Efficient evaluation of quantum observables using entangled measurements. *npj Quantum Information*, 6(1):56, 2020.
- [27] Pranav Gokhale, Olivia Angiuli, Yongshan Ding, Kaiwen Gui, Teague Tomesh, Martin Suchara, Margaret Martonosi, and Frederic T Chong. Optimization of simultaneous measurement for variational quantum eigensolver applications. In *2020 IEEE international conference on Quantum Computing and Engineering (QCE)*, pages 379–390. IEEE, 2020.
- [28] Andrew Zhao, Andrew Tranter, William M Kirby, Shu Fay Ung, Akimasa Miyake, and Peter J Love. Measurement reduction in variational quantum algorithms. *Physical Review A*, 101(6):062322, 2020.
- [29] Linghua Zhu, Senwei Liang, Chao Yang, and Xiaosong Li. Optimizing shot assignment in variational quantum eigensolver measurement. *Journal of Chemical Theory and Computation*, 20(6):2390–2403, 2024.
- [30] Xavier Bonet-Monroig, Ryan Babbush, and Thomas E O'Brien. Nearly optimal measurement scheduling for partial tomography of quantum states. *Physical Review X*, 10(3):031064, 2020.
- [31] Marco Cerezo, Akira Sone, Tyler Volkoff, Lukasz Cincio, and Patrick J Coles. Cost function dependent barren plateaus in shallow parametrized quantum circuits. *Nature communications*, 12(1):1791, 2021.
- [32] Ryan R Ferguson, Luca Dellantonio, A Al Balushi, Karl Jansen, Wolfgang Dür, and Christine A Muschik. Measurement-based variational quantum eigensolver. *Physical review letters*, 126(22):220501, 2021.
- [33] Shu Kanno, Ikko Hamamura, Rudy Raymond, Qi Gao, and Naoki Yamamoto. Efficient implementation of randomized quantum algorithms with dynamic circuits. *arXiv preprint arXiv:2503.17833*, 2025.
- [34] Zhiyan Ding, Xiantao Li, and Lin Lin. Simulating open quantum systems using hamiltonian simulations. *PRX quantum*, 5(2):020332, 2024.
- [35] Elisa Bäumer, Vinay Tripathi, Alireza Seif, Daniel Lidar, and Derek S Wang. Quantum fourier transform using dynamic circuits. *Physical Review Letters*, 133(15):150602, 2024.
- [36] Talal Ahmed Chowdhury, Kwangmin Yu, and Raza Sabbir Sufian. First measurement of entanglement dynamics in the syk model using quantum computers. *arXiv preprint arXiv:2503.18580*, 2025.
- [37] Andrew Zhao, Nicholas C Rubin, and Akimasa Miyake. Fermionic partial tomography via classical shadows. *Physical Review Letters*, 127(11):110504, 2021.
- [38] Gyungmin Cho and Dohun Kim. Entanglement-enhanced randomized measurement in noisy quantum devices. *arXiv preprint arXiv:2504.15698*, 2025.
- [39] Hong-Ye Hu, Andi Gu, Swarnadeep Majumder, Hang Ren, Yipei Zhang, Derek S Wang, Yi-Zhuang You, Zlatko Mineev, Susanne F Yelin, and Alireza Seif. Demonstration of robust and efficient quantum property learning with shallow shadows. *Nature Communications*, 16(1):2943, 2025.
- [40] Christian Bertoni, Jonas Haferkamp, Marcel Hinsche, Marios Ioannou, Jens Eisert, and Hakop Pashayan. Shallow shadows: Expectation estimation using low-depth random clifford circuits. *Physical Review Letters*, 133(2):020602, 2024.
- [41] César Feniou, Olivier Adjoua, Baptiste Claudon, Julien Zylberman, Emmanuel Giner, and Jean-Philip Piquemal. Sparse quantum state preparation for strongly correlated systems. *The Journal of Physical Chemistry Letters*, 15(11):3197–3205, 2024.

- [42] Ho Lun Tang, VO Shkolnikov, George S Barron, Harper R Grimsley, Nicholas J Mayhall, Edwin Barnes, and Sophia E Economou. qubit-adapt-vqe: An adaptive algorithm for constructing hardware-efficient ansätze on a quantum processor. *PRX Quantum*, 2(2):020310, 2021.
- [43] Pierre-Luc Dallaire-Demers and Frank K Wilhelm. Quantum gates and architecture for the quantum simulation of the fermi-hubbard model. *Physical Review A*, 94(6):062304, 2016.
- [44] James B Larsen, Matthew D Grace, Andrew D Baczewski, and Alicia B Magann. Feedback-based quantum algorithms for ground state preparation. *Physical Review Research*, 6(3):033336, 2024.
- [45] Mirko Consiglio, Jacopo Settimo, Andrea Giordano, Carlo Mastroianni, Francesco Plastina, Salvatore Lorenzo, Sabrina Maniscalco, John Goold, and Tony JG Apollaro. Variational gibbs state preparation on noisy intermediate-scale quantum devices. *Physical Review A*, 110(1):012445, 2024.
- [46] Qing Xie, Kazuhiro Seki, and Seiji Yunoki. Variational counterdiabatic driving of the hubbard model for ground-state preparation. *Physical Review B*, 106(15):155153, 2022.
- [47] Ramil Nigmatullin, Kevin Hemery, Khaldoon Ghanem, Steven Moses, Dan Gresh, Peter Siegfried, Michael Mills, Thomas Gatterman, Nathan Hewitt, Etienne Granet, et al. Experimental demonstration of break-even for the compact fermionic encoding. *arXiv preprint arXiv:2409.06789*, 2024.
- [48] Shi Jin and Xiantao Li. A partially random trotter algorithm for quantum hamiltonian simulations. *Communications on Applied Mathematics and Computation*, 7(2):442–469, 2025.
- [49] David Poulin, Matthew B Hastings, Dave Wecker, Nathan Wiebe, Andrew C Doherty, and Matthias Troyer. The trotter step size required for accurate quantum simulation of quantum chemistry. *arXiv preprint arXiv:1406.4920*, 2014.
- [50] Tatsuhiko N Ikeda, Hideki Kono, and Keisuke Fujii. Measuring trotter error and its application to precision-guaranteed hamiltonian simulations. *Physical Review Research*, 6(3):033285, 2024.
- [51] Sergiy Zhuk, Niall F Robertson, and Sergey Bravyi. Trotter error bounds and dynamic multi-product formulas for hamiltonian simulation. *Physical Review Research*, 6(3):033309, 2024.
- [52] Laura Clinton, Johannes Bausch, and Toby Cubitt. Hamiltonian simulation algorithms for near-term quantum hardware. *Nature communications*, 12(1):4989, 2021.
- [53] Antonio D Córcoles, Maika Takita, Ken Inoue, Scott Lekuch, Zlatko K Mineev, Jerry M Chow, and Jay M Gambetta. Exploiting dynamic quantum circuits in a quantum algorithm with superconducting qubits. *Physical Review Letters*, 127(10):100501, 2021.
- [54] Christian Kraglund Andersen, Ants Remm, Stefania Lazar, Sebastian Krinner, Johannes Heinsoo, Jean-Claude Besse, Mihai Gabureac, Andreas Wallraff, and Christopher Eichler. Entanglement stabilization using ancilla-based parity detection and real-time feedback in superconducting circuits. *npj Quantum Information*, 5(1):69, 2019.
- [55] Elisa Bäumer, Vinay Tripathi, Derek S Wang, Patrick Rall, Edward H Chen, Swarnadeep Majumder, Alireza Seif, and Zlatko K Mineev. Efficient long-range entanglement using dynamic circuits. *PRX Quantum*, 5(3):030339, 2024.
- [56] Sergey B Bravyi and Alexei Yu Kitaev. Fermionic quantum computation. *Annals of Physics*, 298(1):210–226, 2002.
- [57] Zhang Jiang, Amir Kalev, Wojciech Mruzekiewicz, and Hartmut Neven. Optimal fermion-to-qubit mapping via ternary trees with applications to reduced quantum states learning. *Quantum*, 4:276, 2020.
- [58] Hsin-Yuan Huang, Richard Kueng, and John Preskill. Information-theoretic bounds on quantum advantage in machine learning. *Physical Review Letters*, 126(19):190505, 2021.
- [59] Scott Aaronson and Daniel Gottesman. Improved simulation of stabilizer circuits. *Physical Review A—Atomic, Molecular, and Optical Physics*, 70(5):052328, 2004.
- [60] Vojtěch Havlíček, Matthias Troyer, and James D Whitfield. Operator locality in the quantum simulation of fermionic models. *Physical Review A*, 95(3):032332, 2017.

**FIGURE LEGENDS**

Figure 1: Circuits for single-copy and two-copy measurements used in our protocols for estimating the dynamical correlation functions. (a) Circuit for single-copy measurements without ancilla qubit (b) Dynamic circuit for single-copy measurements without ancilla qubit (c) Circuit for single-copy measurements with an ancilla qubit (d) Dynamic circuit for single-copy measurements with an ancilla qubit (e) Circuit for two-copy measurements without ancilla qubit (f) Circuit for two-copy measurements with two ancilla qubits